Supporting Information

Bavi et al. 10.1073/pnas.1409011111

SI Materials and Methods

Liposome Preparation and Patch Fluorometry. Liposomes made of azolectin [99.9% (wt/wt)] (P5638; Sigma) and rhodamine-PE [0.1% (wt/wt)] were prepared using a Nanion Vesicle Prep Pro. Briefly, 20 μL of 5 mM lipid dissolved in chloroform and 350 μL of 520 mM D-sorbitol were placed on indium tin oxide (ITO) slides. An alternating electrical field of 5 Hz and 3 V was applied for 120 min to produce liposomes, which were stored at 4 °C. Images of creeping patch membranes were taken using a confocal microscope (LSM 700; Carl Zeiss) equipped with a long working distance water immersion objective (×63; NA 1.15; Carl Zeiss). A 555-nm laser was used to excite the fluorophore and creep of the patch membrane was detected using a long-pass 560-nm filter. Borosilicate glass pipettes (Drummond Scientific) were pulled using a Flaming/Brown pipette puller (P-87; Sutter Instruments) and the tip of each pipette was cut with a microforge (Narishige; MF-900) to a diameter of ∼2 μm. For visualizing the creep, the tip was bent ∼30°, using the microforge to make it parallel to the bottom of the chamber when the pipette was mounted on a micromanipulator (1). Negative pressure steps of −5 mmHg were generated by a High Speed Pressure Clamp-1 apparatus (HSPC-1; ALA Scientific Instruments) and monitored by a piezoelectric pressure transducer (PM015R; World Precision Instruments). To remove adhesion tension, the pipette was filled with 0.1% BSA. After incubation for 30 min at room temperature, the pipette was washed several times with distilled water.

Electrophysiological Experiments. Liposomes were prepared by the dehydration/rehydration (D/R) method (1). Briefly, 2 mg of azolectin lipids (P5638; Sigma) was dissolved in $CHCl_3$, and nitrogen gas was applied to form lipid films. After suspension in 200 μL D/R buffer [200 mM KCl, 5 mM Hepes (pH 7.2, adjusted with KOH)], the solution was subjected to sonication for 5 min to make lipid clouds, and purified MscL protein was added in the ratio of protein to lipid of 1:1,000 (wt/wt). D/R buffer was added up to 3 mL and the mixture was incubated for 1 h, after which biobeads (Bio-Rad) were added and incubated for a further 3 h to remove the detergent. The solution was centrifuged at 250,000 × *g* and the pellet was resuspended in 60 μL D/R buffer, spotted onto a glass slide, and dehydrated under vacuum overnight at 4 °C. The dried film was rehydrated with D/R buffer at 4 °C for 3 h and used for the patch-clamp experiment. The channel currents were amplified with an AxoPatch 1D amplifier (Axon Instruments) and data were acquired at a sampling rate of 5 Hz with 2-kHz filtration in the patch solution [200 mM KCl, 40 mM $MgCl_2$, and 5 mM Hepes (pH 7.2, adjusted with KOH)]. Pressure was applied manually with a syringe for flare-up experiments; ramp pressures were generated by a High Speed Pressure Clamp-1 apparatus (HSPC-1; ALA Scientific Instruments).

Finite-Element Simulation. Finite-element (FE) simulation has been used widely to model the micropipette aspiration technique to study the mechanical behavior of several different cell types (2–6). Given the geometric nonlinearities that had to be taken into consideration, we used commercial finite-element analysis (FEA) software (Abaqus/Standard; Dassault Systems Simulia) for simulations as well as for prediction of the stress and strain distribution in azolectin liposomes and excised membrane patches exposed to pipette aspiration. As the inertial forces were negligible during suction, the procedure was considered quasistatic. The lipid vesicles were assumed to be deformable thin-walled spheres for cell-attached configuration (Fig. S1*A*). Thin L-shaped shells were used for the excised patch configuration (Fig. S1 *B* and *C*). All models had a thickness of 3.5 nm (unless otherwise specified), having isotropic and homogeneous material properties, for which the bending deformations are important. Hence, internal pressure causes negligible stretching and shell permeability is less important to the deformation (7) (Fig. S1). We used shell theory for our computational model, because a shell element can sustain bending moments and maintain irregular geometry. Membrane theory failed to explain the deformation of the lipid bilayer under aspirating pressure for either cell-attached or excised patch configurations. This is because, by definition, a membrane cannot sustain a bending moment. Thus, irregular undulations on the membrane surface cannot remain stable without proper constraints. In fact, when membrane elements were used for typical patch geometries, we could not converge to a solution under any reasonable load. Further, even in very low pressures, the patch deforms like a bell rather than having a parabolic or hemispheric shape (typical shapes that can be found in typical experiments). The two-node SAX1 element was used, which is two-node stress/displacement element that uses one point integration of the linear interpolation function for the distribution of loads (ABAQUS 6.11-2). The FE model consisted of 297 and 112 linear axisymmetric elements (SAX1) for the cell-attached and excised patch configurations, respectively. Sensitivity to mesh density (total number of elements and nodes in the computational model) was also studied, meaning the original model was remeshed to obtain meshes of different density. The results were seen to be independent of mesh size, beyond the number of elements stated for each FE model. Our results were also independent of the type of element. For instance, the quadratic three-node element, SAX2, could also be used. Although compared with SAX1 elements, a lower number of SAX2 elements are needed to converge to the results, the chance of simulation abortion (due to severe distortion of elements) was seen to be much higher for SAX2. A finer mesh (maximum aspect ratio of ∼1:7) was used in the current study to accommodate the highly curved geometry near the pipette tip and to avoid distortion of elements. Due to the axisymmetric feature of the problem, we modeled an axisymmetric wire in our FE model. A fillet radius was considered at the opening of the micropipette to mimic the experimentally used micropipettes and to reduce element distortion that would prevent termination of the FE computation (Fig. S1*A*). Moreover, the fillet radius appeared to have no significant effect on the results as long as the pipette was large enough (3). Symmetrical boundary conditions were used on the liposome, restricting its horizontal movement in the axis of symmetry. As illustrated in Fig. S1, because the micropipette was significantly stiffer than the liposomes, the micropipette was assumed to be rigid and fixed at its reference point (restricted from moving in all translational and rotational directions). Frictionless, hard contact (penalty method), finite sliding, surface-to-surface contact was implemented between the micropipette and the liposome surface. For patch fluorometry experiments in all FE simulations, suction was increased from 0 to its maximum value within 0.05 s for each step. ABAQUS requires Young's modulus, E, and the Poisson ratio, ν, for elastic models, and neo-Hookean material parameters can be expressed in terms of C_{10} and $D1$. E and C_{10} could be obtained experimentally and ν and $D1$ were assumed to be 0.5 and 0, respectively, as lipid bilayers can be considered as almost incompressible materials (8–12). All these values are stated in the relevant legends for each FE simulation.

For viscoelastic materials, ABAQUS uses a Prony series expansion of the dimensionless relaxation modulus. ABAQUS inputs for

viscosity are shear relaxation modulus ratio, bulk modulus, and relaxation time. A parametric set of simulations has been performed. Assuming lipid bilayers as incompressible materials, wide ranges of shear relaxation modulus ratio, g_i (0.1–0.9), and relaxation time, tau_i (10 μs to 1 s), have been considered in our simulations to cover the rheometry of different lipids with different characteristics. When we increase g_i, it means that the long-term shear modulus decreases (more fluid behavior) and if we decrease tau_i, we reduce the rate of transition from the short-term to the long-term modulus. The ABAQUS Analysis User's Manual covers viscoelasticity in detail.

Micropipette Aspiration Technique (Constitutive Model Based on an Equibiaxial Tension Assumption for Liposome Elongation in the Pipette, Model 1). A popular structural model for liposomes assumes that they have mostly elastic behavior. They cannot be simply modeled as a thin liquid film because the hydrocarbon-chain interior of the membrane exhibits elastic behavior when its thickness is varied (13). The use of static analysis was justified here because the timescale of relaxation from viscoelastic effects is on the order of tens of microseconds (10, 14).

During deformation, lipid bilayers bear external loads and resist bending deformation. Membrane mechanical properties have been extensively studied by application of pressure across an aspirated liposome in a glass pipette (micropipette aspiration technique). In those experiments, however, the lipid glass adhesion and seal formation were overlooked (10, 15, 16). Thus, the traditional analytical model used to estimate membrane tension in stretched membrane patches based on Laplace's law had to be modified with regard to the radius of the liposome patch to calculate accurately the membrane tension, T. The membrane tension in the presence of the adhesion tension is expressed as (17, 18)

$$T = \frac{PR_d}{2(1 - R_d/R_v)}. \qquad \textbf{[S1]}$$

This equation was applied to both the portion of the vesicle inside the micropipette with the inner radius of R_p and that outside the pipette with the radius of R_v. P is the pressure difference between the outside and the inside of the patch; R_d is the local radius of curvature of the patch area, which is equal to $(R_p^2 + h^2)/2h$, and h is the height of the patch dome (Fig. S1 *D*–*F*). In the absence of the adhesion tension, a simpler form of Eq. **S1** can be derived for micropipette analysis, where $R_d = R_p$ (7, 15). Obviously the stretching modulus resulting from Eq. **S1** will be higher than the resulting stretching modulus when we use $T = PR_p/2(1 - R_p/R_v)$ to calculate the tension. This is because R_d is always greater than R_p. Thus, for the same strain, higher values of T were obtained at the corresponding tensions.

The resulting membrane strain, α, which is the area change, ΔA, normalized by the initial area, A_0, was calculated as follows:

$$\alpha = \frac{\Delta A}{A_0} \sim \frac{1}{2}\left(\left(\frac{R_p}{R}\right)^2 - \left(\frac{R_p}{R}\right)^3\right)\frac{\Delta L}{R_p}. \qquad \textbf{[S2]}$$

ΔL is the change in projection length produced by an increase in applied pressure (Fig. S1). Eq. **S2** was deduced with the viable assumption that the internal volume of the vesicle during micropipette aspiration remains constant due to incompressibility of aqueous solution inside the vesicle (15, 19). Following a typical micropipette aspiration protocol, the area stretch elasticity modulus under a high membrane tension regime [when $T > 0.5$ mN/m (20, 21)], K_A, was calculated as follows:

$$K_A = \frac{\Delta T}{\alpha}. \qquad \textbf{[S3]}$$

ΔT is the change in tension due to the change of negative pressure at each pressure step. Depending on the thickness of the lipid bilayer, we can relate the area stretch elasticity to Young's modulus, using the following expression (Fig. S2*A*):

$$E = \frac{2K_A(1 - \nu)}{t}. \qquad \textbf{[S4]}$$

In cases of uniform stretching and bending, the bilayer behaves as an incompressible elastic body (13). Thus, ν is the Poisson ratio that can be assumed to be near 0.5 (8–11) and t is the thickness of the unstressed lipid bilayer. For lipid bilayers (assuming uniform lateral pressure distribution with depth in the uncoupled monolayers), the elastic modulus is related to the bending rigidity, k_b, through $k_b = Et^3/24$, where t is the bilayer thickness (10, 22, 23).

Constitutive Model Based on Uniaxial Linear Elastic Assumption (Model 2). Although the patch fluorometry experiment did not exhibit all ideal uniaxial test conditions, one could consider this experiment as a uniaxial test. If we look at the liposome behavior on the patch scale (>1 μm, range of pipette radius) rather than on the lipid raft scale (10–200 nm) (24), the cylindrical pipette precludes expansion of lipid in the radial direction. Hence, a uniaxial assumption was more appropriate than an equibiaxial assumption for obtaining a stress–strain curve of the lipid during patch fluorometry experiments. In both the traditional and the alternative models, it was assumed that there was no substantial slippage of the lipid molecules from outside the pipette into the pipette during suction (after the initial equilibrium position). Moreover, the effect of the normal force that the pipette exerted on the lipid inside the pipette was disregarded. Although the azolectin lipid showed almost linear elastic behavior, to improve the accuracy of our calculations, the nominal longitudinal strain was linearized as

$$\varepsilon_i = \varepsilon_{i-1} + \frac{\Delta L_i}{L_{i-1}} \quad (\varepsilon_0 = 0 \text{ and } i = 1, 2, 3, 4), \qquad \textbf{[S5]}$$

where L_0 is the initial projection length and ΔL_i is the change of corresponding projection lengths at each pressure step. Using Eq. **S1**, the nominal tensile stress was also calculated as

$$\sigma = \frac{T}{t}. \qquad \textbf{[S6]}$$

From the slopes of the plots of the applied tension vs. the nominal longitudinal strain of all of the experimental data obtained in this study, Young's modulus of azolectin lipid could be calculated (Fig. S2*B*).

Large-Strain Isotropic Hyperelastic Constitutive Model (Model 3). It is important to mention that a hyperelastic material is still an elastic material, which means that it returns to its original form after deformation forces have been removed. The linear elastic coefficients of azolectin liposomes were discussed in the previous section. Given that elastic material models are intended for elastic strains that usually remain small (<5%) and hyperelastic material models are more appropriate for most biological materials, particularly at large strain magnitudes (>5%) (25), we fitted a hyperelastic model to our experimental data and introduced the corresponding coefficients. In fact, herein we show that liposomes could be modeled as a large-strain isotropic hyperelastic material. Hyperelastic materials also are Cauchy elastic, which means that

the stress is determined by the current state of deformation, not by the path or history of deformation. The Cauchy stress can be derived from the strain energy function, which is given by (26)

$$U=\sum_{i+j=1}^{N} C_{ij}\left(\bar{I}_1-3\right)^i\left(\bar{I}_2-3\right)^j+\sum_{i=1}^{N}\frac{1}{D_i}\left(J^{\mathrm{el}}-1\right)^{2i} \qquad \textbf{[S7]}$$

(Deviatoric part) (Volumetric part),

where U is the strain energy per unit of reference volume and i and j are integer numbers. As shown in Eq. **S7**, U contains a deviatoric part and a volumetric part. N is the polynomial order, C_{ij} and D_i are temperature-dependent material parameters, $\bar{I}_i$ are deviatoric strain invariants of the left Cauchy–Green deformation tensor, and J^{el} is the elastic volume ratio. In this section we summarize briefly the equations of incompressible isotropic nonlinear elasticity that are required for comparing the theory with patch fluorometry data. We assume homogeneous deformations that can be classified as pure homogeneous strain, i.e., deformations of the form

$$x_1=\lambda_1 X_1,\quad x_2=\lambda_2 X_2,\quad x_3=\lambda_3 X_3, \qquad \textbf{[S8]}$$

where X_1, X_2, and X_3 are rectangular Cartesian coordinates that identify material particles in some unstressed reference configuration. x_1, x_2, and x_3 are the corresponding coordinates after deformation with respect to the same axes. $\lambda_i(i=1,2,3)$ are the stretch ratios in the principal directions. The first and second deviatoric strain invariants in Eq. **S7** are defined as

$$\bar{I}_1=\lambda_1^2+\lambda_2^2+\lambda_3^2,\quad \bar{I}_2=\lambda_1^2\lambda_2^2+\lambda_2^2\lambda_3^2+\lambda_1^2\lambda_3^2. \qquad \textbf{[S9]}$$

The principal stretch ratios $\lambda_i(i=1,2,3)$ are related to the principal nominal strain ε_i through $\varepsilon_i=\lambda_i-1$. The principal stretch λ_i can be linearized, as previously explained in Eq. **S5**, to achieve more accuracy. With the assumption of full incompressibility for lipid membranes (7),

$$J^{\mathrm{el}}=\lambda_1\lambda_2\lambda_3=1. \qquad \textbf{[S10]}$$

Thus, the volumetric part of strain energy (U) becomes equal to zero. The principal Cauchy stresses σ_i $(i=1,2,3)$ [defined as force per unit deformed cross-sectional area normal to the x_i $(i=1,2,3)$ axis in the deformed configuration] are related to the stretches through U according to the equations

$$\sigma_i=\lambda_i\frac{\partial U}{\partial\lambda_i}-P\quad i=1,2,3. \qquad \textbf{[S11]}$$

However, for calculation of the Cauchy stresses, we need to know the exact thickness at different parts of the patch area during aspiration of the liposomes. To avoid this at this juncture, the corresponding nominal stresses (defined as per unit undeformed cross-sectional area) are the stresses that are often measured directly in experiments and thus are given by (26)

$$\sigma_i=\frac{\partial U}{\partial\lambda_i}-P\lambda_i^{-1}\quad i=1,2,3. \qquad \textbf{[S12]}$$

For an incompressible material it is always possible to superimpose a hydrostatic stress without producing strain and Eq. **S12** changes to

$$\sigma_i=\frac{\partial U}{\partial\lambda_i}\quad i=1,2,3. \qquad \textbf{[S13]}$$

As presented in the following sections, the results show linear behavior for azolectin lipid bilayer (Fig. S2), and we were unable to perform enough different standard experiments on the liposome vesicles (because of their sensitive properties, size, and form). Here we use the simplest constitutive model, the neo-Hookean model. The neo-Hookean model is the first-order polynomial form of the general hyperelastic model with $N=1$. It uses only linear functions of the invariants. In this model, the strain energy density is a linear function of deviatoric strain invariants, $\bar{I}_1$ and $\bar{I}_2$, and can be derived from Eq. **S7** as follows:

$$U=C_{10}\left(\bar{I}_1-3\right). \qquad \textbf{[S14]}$$

In the neo-Hookean model, shear modulus, G, is

$$G=2C_{10}. \qquad \textbf{[S15]}$$

As a result, we may simplify the boundary and loading conditions inside the pipette as illustrated in Fig. S3. Also the geometry and membrane stresses of the lipid bilayer during a micropipette aspiration experiment are indicated. R_P and σ represent the inner radius of the pipette and the longitudinal stress of the membrane, respectively. L is the length of projection of the lipid inside the micropipette. λ_1 and λ_2 are the stretching ratios in directions 1 (horizontal) and 2 (vertical), respectively. Fig. S3, *Right* depicts the planar form of a liposome with the associated boundary conditions caused by the rigid micropipette. The rigid cylindrical pipette around the patch area prevents any growth of the radius in the portion of the liposome within the pipette, $\lambda_1=1$ (Fig. S3). Also, due to the boundary conditions of the liposome bilayer within the pipette and the incompressibility of azolectin lipid, $\lambda_3=1/\lambda_2=1/\lambda$. Hence, Eq. **S14** can be expressed in terms of λ as

$$U=\frac{G}{2}\left(\lambda^2+\frac{1}{\lambda^2}-2\right). \qquad \textbf{[S16]}$$

Thus, using Eq. **S13**, the nominal stress in the main direction 2 can be expressed as

$$\sigma=G\left(\lambda-\frac{1}{\lambda^3}\right), \qquad \textbf{[S17]}$$

where $\sigma=T/t$ ($t=3.5$ nm). T can be calculated from Eq. **S1**. The slope of the nominal stress and $\lambda-1/\lambda^3$ indicate the shear modulus (Fig. 1*C*).

Equations for Excised Patch Configuration. To suppress unknown thermodynamic effects such as membrane pretension (27) and thermal undulations (19–21) involved in the mechanical behavior of liposomes and, more importantly, to study the rheological behavior of the lipid in the excised patch configuration, micropipette aspiration was performed on three different excised patches (Fig. 3). This method has several advantages over the cell-attached configuration, including simplicity and accuracy. For tension in the excised patch membrane, T, in Eq. **S1**, based on a principle of surface chemistry (Laplace's law) is changed as follows (12, 27–31):

$$T=\frac{PR_d}{2}. \qquad \textbf{[S18]}$$

R_d is the radius of curvature of the patch (Fig. S1 *D–F*). Note that there is no attached liposome part in the excised patch configuration. Therefore, the fundamental assumption of a conserved internal volume for the vesicle due to the incompressibility of the water inside the liposome during micropipette aspiration is no longer viable. Membrane deformations in excised patch experiments are conventionally characterized by the relative change

in the visible area measured with respect to a somewhat arbitrarily chosen initial state area, A_0. The areal strain (fractional area change) is defined by

$$\alpha = \frac{A - A_0}{A_0}, \qquad \textbf{[S19]}$$

where A is the total deformed area of the patch. Using very basic geometric relations, the deformed area can be calculated from the cylindrical length, L; the pipette radius, R_p; and the height of the dome of the patch, h (Fig. 3) by

$$A = 2\pi R_p L + \pi\left(R_p^2 + h^2\right). \qquad \textbf{[S20]}$$

Because the other models discussed in this paper (uniaxial and hyperelastic models) do not deal with the attached part of the vesicle in the cell-attached configuration (and thus the constant volume assumption), they are all still valid also for the excised patch configuration. In those models, however, for the calculation of membrane tension, Eq. **S18** should be used instead of Eq. **S1**. The material properties obtained from different models (models 1–3) for excised patch configuration are demonstrated (Fig. S4 and Fig. 3*C*).

Supporting Patch Fluorometry Data Without Adhesion Tension. To calculate the bilayer material properties (i.e., K_A) we used ΔT, which is the change in tension due to the change of negative pressure at each pressure step (Eq. **S3**). We believe this reduces the potential influence of adhesion tension, assuming this value stays constant during pressure application. Furthermore, we carried out additional patch-fluorometry experiments, using BSA to reduce adhesion tension. As mentioned in the literature, we used 0.02% BSA (32) and the result was similar to what we previously measured. However, this concentration failed to completely remove adhesion tension. Using only 0.1% BSA allowed complete removal of adhesion tension (Movie S5). The corresponding value calculated for K_A using model 1 is ~91 mN/m, which is similar to that calculated in the absence of BSA (~112 mN/m; Table 1). The corresponding value of K_A using model 3 is 10 mN/m (~14 mN/m without BSA; Table 1), given that 0.1% might affect the membrane properties and increase the irreproducibility of K_A (32–35).

Thus, a small amount of adhesion tension aids experimental simplicity and is likely present in a large number of the published micropipette aspiration (MA) reports, which is signified clearly by the radius of curvature being larger than the radius of the pipette, which can be seen in the initial equilibrium state of the patch in previous studies (7, 21, 36). Importantly, this adhesion tension does not seem to affect our calculated values for K_A.

Supporting Computational Data. As mentioned, shell theory was used in our computations, which is a more advanced theory for estimation of tension in thin-walled shells compared with Laplace's law. The spatial profiles of the aspirated liposome calculated by the FE simulation are presented in Fig. 2 *A* and *B* and Fig. S5. The vesicle has a diameter of 6.2 μm with the inner diameter of the micropipette being 2.8 μm (both are typical sizes encountered experimentally). The suction begins from 0 and reaches a value of –30 mmHg (~4 kPa), instantaneously (in 0.01 s), and is then kept constant for 0.01 s. The computations were performed for the material parameters of $C_{10} = 0.5$ MPa and $k_b = 5.36 \times 10^{-21}$ (neo-Hookean model). The in-plane maximum and effective (von Mises) stress fields are represented in Fig. 2 *A* and *B*. Von Mises stress, S_v, is an equivalent stress of distortion energy of a material, which in principal directions can be calculated from

$$S_v = \sqrt{\frac{(S_1 - S_2)^2 + (S_1 - S_3)^2 + (S_1 - S_2)^2}{2}}, \qquad \textbf{[S21]}$$

where S_i (i = 1, 2, 3) are the stress components in the principal directions. Von Mises stress is used for fracture analysis of ductile materials. The stress distributions were nonuniform, with continuous regions of high and low stress. Moreover, to distinguish the role of the rigid micropipette in the movement of lipid molecules during micropipette aspiration, the vertical displacement field and in-plane maximum principal strain field in the azolectin vesicle were calculated and are shown in Fig. S5. By comparing the vertical displacement field and the in-plane maximum principal strain field it can be observed that, although the apex of the patch has the largest vertical displacement, the elements within the liposome–pipette normal contact region have the greatest strains (Fig. S5). This implies that when a local stress is produced in this area, the lipid membrane is unable to reconfigure itself and reduce the strain. Consequently, movement of the elements (in an FE simulation) or the phospholipids of the membrane (in reality) (10) is restricted and this facilitates membrane rupture (Figs. S3 and S5). The computational results show that the response is mostly dominated by local stretching of the liposome rather than its shear and/or bending effects near this normal contact area. No substantial result sensitivity to the contact conditions between the liposome and the pipette is observed, as the stress and the resulting deformation are mainly dominated by force regime and longitudinal movement of membrane within the pipette rather than by normal and tangential effects near the pipette opening.

A set of FE computations was performed to study the effects of the radius of the vesicle on tension, thickness variation, and in-plane stress field of the patch in the cell-attached configuration (Fig. S6). The vesicle size ranged from 3.1 μm (small vesicles that could be found abundantly in each sample) to 12.4 μm (rare typical sizes encountered experimentally). We showed that the radius of the vesicle outside liposome had no substantial effect on tension distribution, thickness variation, and stress field in the patch area within the pipette (Fig. S6). This is consistent with what we had assumed for deducing our mathematical elastic and hyperelastic equations. The tensions estimated from the Laplace equation for the cell-attached configuration (Eq. **S1**) and the excised patch configuration (Eq. **S18**) were compared with the FE results. On the basis of our computational results, for relatively small vesicles (i.e., $R_v < 9$ μm) the estimated tension obtained from Eq. **S1** is always an overestimation. On the other hand, for larger vesicles, like the tension estimated from Eq. **S18**, the results were always lower than the (FE) values (Fig. 2*D*). This also allowed us to choose the more appropriate equation (between Eqs. **S1** and **S18**) for tension estimation in the process of calculating the mechanical properties of lipid bilayer.

Previously, we showed that a micropipette aspiration protocol based on an equibiaxial tension assumption results in overestimation of lipid elastic moduli. Moreover, the mechanical properties of larger liposomes are shown to be stiffer than those of smaller vesicles. However, unlike the cell-attached configuration, the mechanical properties obtained from an isolated patch in micropipette aspiration (excised patch configuration) are very similar using all three different material models (Fig. S4 *A* and *B*, Fig. 3*B*, and Table S2). In a similar manner to that performed for the cell-attached configuration, we also modeled the excised patch experiment (Fig. S1 *B* and *C*). The mechanical properties obtained were used as input data for our computational model to see whether we could observe the same rheological behavior for our lipid bilayer model under experimental conditions (i.e., typical patch and pipette geometry in conjunction with similar load and boundary conditions). Thus, the length of lipid membrane

within the pipette at four different pressures was compared with experimentally derived values and very good agreement was found between the two approaches (Fig. S4 *C* and *D* and Fig. 3*C*). We believe that the relatively small difference between the two is mainly attributable to the adhesion tension between lipid and micropipette, which was not taken into account in our computational model.

Both typical pipette shapes, cylindrical and tapering, were simulated to see whether there was any difference in rheological behavior between the two during aspiration. Furthermore, a set of calculations was performed, considering similar computational conditions to indicate the effect of initial membrane thickness on the maximum membrane stress (in the apex of the patch), up to suction pressure 40 mmHg (Figs. S7 and S8). The initial thickness of the lipid bilayer did not affect the tension distribution but it had a considerable effect on the membrane stress distribution within the patch area. The thinner the membrane, the higher was the stress at any given pressure.

Effect of Membrane Fluidity (Internal Dissipation) on the Stress–Strain Distribution of Patched Lipid Bilayers. Visco-hyperelasticity is the property of materials that exhibit both viscous and hyperelastic characteristics when undergoing large deformation. Given that fluid–lipid biomembranes show both liquid-like and solid-like behavior, numerous researchers have adopted viscoelastic models for describing the behavior of different lipid bilayers and cell membranes (3, 6, 14, 37–42).

Although for azolectin we and others (1) have seen negligible stiffness nonlinearity (Figs. 1*C* and 3*B* and Figs. S2 and S4 *A* and *B*) and hysteresis (Movie S5), we considered a low viscous (fluidic) behavior for lipids in addition to the lipid hyperelasticity to see how this changes the stress distribution in the patch area. In other words, a hyperelasticity model was used to study the result of the reversible bond stretching along the crystallographic planes of the lipid bilayer. Herein, viscosity was added to our previous (hyperelastic) model to capture the influence of the fluidity (internal damping) and creep of lipid molecules inside the pipette during micropipette aspiration. This enabled us to investigate the influence of lipid internal viscosity on the stress–strain distribution within the patch area during micropipette aspiration of the bilayer.

In the previous hyperplastic model (Figs. 2 and 3), the results from finite-element simulations predict that there is a persistent heterogeneity in tension with the maximum at the top of the patch dome of highly viscous membranes. In our introduced alternative visco-hyperelastic model, we assume a surface viscosity as the internal dissipative mechanisms of the bilayer. Our results indicate that for the membranes with low viscosity (high fluidity), such nonuniform distribution of tension is still feasible for different loading conditions (step or ramp), various fluidities, and typical experimental time courses. In a time course of 5 s (a typical experimental time) the maximum tension in the patch starts to expand over the patch area due to the relaxation along the tension gradient (Movies S6 and S7). This happens in both cell-attached and excised bilayer models. As shown, after 5 s the difference between the stress in the dome (maximum) and the stress near the wall (minimum) is about 50% (Movie S6). Hence, comparing results from the visco-hyperelastic model with our previous results, not only is the heterogeneous distribution of the stress valid with the existence of membrane fluidity but also it introduces a new time-dependent axisymmetric growth of the high-stress region (at the patch center) toward the low-stress area (near the pipette wall). This tense area in the center of the patch develops to the sides of the patch area (adjacent to the pipette wall) as the lipid creeps inside the pipette during the simulated experimental time. Thus, stress heterogeneity is valid for a wide range of instantaneous and long-term shear modulus and relaxation times.

Effect of Intermonolayer Dissipation: Modeling the Bilayer as Two Sliding Slabs. Previous models (models 1–3) were conceptualized on the basis of the mechanical behavior for a unit membrane structure for simplicity. This assumption is quite viable when there is a rapid displacement between layers (i.e., applying instantaneous suction). In this case, their relative lateral motion will be opposed by a considerable viscous drag at the bilayer midplane, which will lead to "dynamic coupling" of the monolayers, causing them to behave as a single slab (43). However, the monolayers are able to slide one relative to another in the case of regular displacements. This is because monolayers are tied together by a weak van der Waals (vdw) attraction at the midplane, stemming from the aqueous half spaces surrounding the bilayer (43).

Given that the boundary and loading conditions are different between the monolayers during micropipette aspiration, herein, we examine to what extent this affects the stress distribution between the monolayers in both cell-attached and excised configurations. The interlayer drag has been assumed to be velocity dependent and it follows the postulated constitutive relation for interlayer coupling $\tau = b\Delta v_s$. This assumption has been used in many other continuum mechanics (coarse grain) models of lipid bilayers, where b represents the magnitude of coupling embodied in a constant drag coefficient (of order 10^8 $N-$ s/m^3). Δv_s represents the relative rate that molecules (nodes in our continuum model) in opposite monolayers slip past each other as the bilayer deforms (43).

As mentioned before, the monolayers are in contact with each other via a weak force stemming from vdw interaction between the two hydrophobic surfaces. The interlayer pressure as a function of the distance can be computed, adopting the vdw stress between two parallel bilayers,

$$S = \frac{-A_H}{6\pi D^3}. \qquad \text{[S22]}$$

Here S is the stress, A_H is the Hamaker constant, and D is the distance between the two monolayers. For lipid bilayers in water the Hamaker constant is $\sim 5\ (\pm 2) \times 10^{-21}$ J (7, 44). Let us consider this number for hydrocarbons in the monolayers. The normal tractions can be positive, indicating an attractive interaction between the surfaces, or negative, in the case of repulsive forces.

The resulting expression of the interlayer contact interactions has been implemented in an ABAQUS user subroutine for simulating the vdw force. In ABAQUS/Standard, user subroutine UINTER can be used to define the constitutive interaction between two deforming surfaces. Monolayers are defined as the master and slave surfaces, and the UINTER is called for each slave node at each time increment of the analysis. Inputs to this subroutine are the initial and incremental relative positions of each slave node with respect to its closest point on the master surface and the material properties defined for the monolayers. The constitutive calculation thus involves computing the tractions based on the increments in relative position of the slave node with respect to the master surface.

Interestingly, our results indicate that higher membrane stress values are developed in the outer leaflet compared with the inner one by considering the lipid bilayer as two sliding surfaces. The asymmetry in the stress profiles of the two leaflets exists in both excised and cell-attached systems. However, we showed that for similar characteristics and conditions, the dissimilarity between the stress profiles of two monolayers is much more noticeable in the excised configuration compared with the cell-attached one. In the excised patch system, the maximum stress that arises in the upper monolayer (the one that is in contact with the pipette) is about 30% larger than the maximum stress in the inner monolayer (Fig. 3 *D* and *E*), whereas in the cell-attached configuration, the difference in the monolayers' maximum stress is less than 2% (Fig. 2 *E* and *F*). The difference between the monolayers stems

from the fact that the inner leaflet in the excised patch has a higher degree of freedom for lateral movement and relaxation than the inner leaflet in the cell-attached conformation. Based on these results, we can suggest that depending on the location of the pore in different MS channels (close to or away from the midplane), the dissimilarity between the distributed stresses in the monolayers can affect activation of MS channels reconstituted and investigated in an excised patch system (45, 46).

1. Nomura T, et al. (2012) Differential effects of lipids and lyso-lipids on the mechanosensitivity of the mechanosensitive channels MscL and MscS. *Proc Natl Acad Sci USA* 109(22):8770–8775.
2. Sato M, Theret DP, Wheeler LT, Ohshima N, Nerem RM (1990) Application of the micropipette technique to the measurement of cultured porcine aortic endothelial cell viscoelastic properties. *J Biomech Eng* 112(3):263–268.
3. Vaziri A, Mofrad MR (2007) Mechanics and deformation of the nucleus in micropipette aspiration experiment. *J Biomech* 40(9):2053–2062.
4. Jafari Bidhendi A, Korhonen RK (2012) A finite element study of micropipette aspiration of single cells: Effect of compressibility. *Comput Math Methods Med* 2012, 10.1155/2012/192618.
5. Zhou E, Lim C, Quek S (2005) Finite element simulation of the micropipette aspiration of a living cell undergoing large viscoelastic deformation. *Mech Adv Mater Structures* 12(6):501–512.
6. Trickey WR, Baaijens FP, Laursen TA, Alexopoulos LG, Guilak F (2006) Determination of the Poisson's ratio of the cell: Recovery properties of chondrocytes after release from complete micropipette aspiration. *J Biomech* 39(1):78–87.
7. Evans E, Needham D (1987) Physical properties of surfactant bilayer membranes: Thermal transitions, elasticity, rigidity, cohesion and colloidal interactions. *J Phys Chem* 91(16):4219–4228.
8. Kirk GL, Gruner SM, Stein D (1984) A thermodynamic model of the lamellar to inverse hexagonal phase transition of lipid membrane-water systems. *Biochemistry* 23(6): 1093–1102.
9. Kuzmin PI, Akimov SA, Chizmadzhev YA, Zimmerberg J, Cohen FS (2005) Line tension and interaction energies of membrane rafts calculated from lipid splay and tilt. *Biophys J* 88(2):1120–1133.
10. Rodowicz KA, Francisco H, Layton B (2010) Determination of the mechanical properties of DOPC:DOPS liposomes using an image procession algorithm and micropipette-aspiration techniques. *Chem Phys Lipids* 163(8):787–793.
11. Akimov SA, Kuzmin PI, Zimmerberg J, Cohen FS (2007) Lateral tension increases the line tension between two domains in a lipid bilayer membrane. *Phys Rev E Stat Nonlin Soft Matter Phys* 75(1 Pt 1):011919.
12. Hamill OP, Martinac B (2001) Molecular basis of mechanotransduction in living cells. *Physiol Rev* 81(2):685–740.
13. Kralchevsky PA, Paunov VN, Denkov ND, Nagayama K (1995) Stresses in lipid membranes and interactions between inclusions. *J Chem Soc Faraday Trans* 91(19): 3415–3432.
14. Earnshaw JC, Crawford GE (1989) Viscoelastic relaxation of bilayer lipid membranes: II. Temperature dependence of relaxation time. *Biophys J* 55(5):1017–1021.
15. Evans E, Rawicz W (1997) Elasticity of "fuzzy'" biomembranes. *Phys Rev Lett* 79(12): 2379–2382.
16. Kwok R, Evans E (1981) Thermoelasticity of large lecithin bilayer vesicles. *Biophys J* 35(3):637–652.
17. Mitchison J, Swann M (1954) The mechanical properties of the cell surface I. The cell elastimeter. *J Exp Biol* 31(3):443–460.
18. Bowman CL, Gottlieb PA, Suchyna TM, Murphy YK, Sachs F (2007) Mechanosensitive ion channels and the peptide inhibitor GsMTx-4: History, properties, mechanisms and pharmacology. *Toxicon* 49(2):249–270.
19. Henriksen JR, Ipsen JH (2004) Measurement of membrane elasticity by micro-pipette aspiration. *Eur Phys J E Soft Matter* 14(2):149–167.
20. Needham D, Nunn RS (1990) Elastic deformation and failure of lipid bilayer membranes containing cholesterol. *Biophys J* 58(4):997–1009.
21. Rawicz W, Olbrich KC, McIntosh T, Needham D, Evans E (2000) Effect of chain length and unsaturation on elasticity of lipid bilayers. *Biophys J* 79(1):328–339.
22. Allen KB, Layton BE (2009) Determination of the forces imposed by micro and nanopipettes during DOPC: DOPS liposome manipulation. *Chem Phys Lipids* 162(1–2): 34–52.
23. Bloom M, Evans E, Mouritsen OG (1991) Physical properties of the fluid lipid-bilayer component of cell membranes: A perspective. *Q Rev Biophys* 24(3):293–397.
24. Lingwood D, Simons K (2010) Lipid rafts as a membrane-organizing principle. *Science* 327(5961):46–50.
25. Holzapfel GA, Ogden RW (2006) *Mechanics of Biological Tissue* (Springer, Berlin).
26. Ogden R, Saccomandi G, Sgura I (2004) Fitting hyperelastic models to experimental data. *Comput Mech* 34(6):484–502.
27. White SH (1980) Small phospholipid vesicles: Internal pressure, surface tension, and surface free energy. *Proc Natl Acad Sci USA* 77(7):4048–4050.
28. Tanford C (1979) Hydrostatic pressure in small phospholipid vesicles. *Proc Natl Acad Sci USA* 76(7):3318–3319.
29. Opsahl LR, Webb WW (1994) Lipid-glass adhesion in giga-sealed patch-clamped membranes. *Biophys J* 66(1):75–79.
30. Suchyna TM, Markin VS, Sachs F (2009) Biophysics and structure of the patch and the gigaseal. *Biophys J* 97(3):738–747.
31. Ursell T, Agrawal A, Phillips R (2011) Lipid bilayer mechanics in a pipette with glass-bilayer adhesion. *Biophys J* 101(8):1913–1920.
32. Zhou Y, Raphael RM (2005) Effect of salicylate on the elasticity, bending stiffness, and strength of SOPC membranes. *Biophys J* 89(3):1789–1801.
33. Shoemaker SD, Vanderlick TK (2002) Intramembrane electrostatic interactions destabilize lipid vesicles. *Biophys J* 83(4):2007–2014.
34. Wu Y, Fletcher GL (2000) Efficacy of antifreeze protein types in protecting liposome membrane integrity depends on phospholipid class. *Biochim Biophys Acta* 1524(1): 11–16.
35. Yokouchi Y, et al. (2001) Effect of adsorption of bovine serum albumin on liposomal membrane characteristics. *Colloids Surf B Biointerfaces* 20(2):95–103.
36. Evans E, Rawicz W, Smith BA (2013) Back to the future: Mechanics and thermodynamics of lipid biomembranes. *Faraday Discuss* 161:591–611.
37. Waugh R, Evans EA (1976) Viscoelastic properties of erythrocyte membranes of different vertebrate animals. *Microvasc Res* 12(3):291–304.
38. Jamali Y, Azimi M, Mofrad MR (2010) A sub-cellular viscoelastic model for cell population mechanics. *PLoS ONE* 5(8):pii:e12097.
39. Canham PB (1970) The minimum energy of bending as a possible explanation of the biconcave shape of the human red blood cell. *J Theor Biol* 26(1):61–81.
40. Mills JP, Qie L, Dao M, Lim CT, Suresh S (2004) Nonlinear elastic and viscoelastic deformation of the human red blood cell with optical tweezers. *Mech Chem Biosyst* 1(3):169–180.
41. Lubarda V, Marzani A (2009) Viscoelastic response of thin membranes with application to red blood cells. *Acta Mech* 202(1–4):1–16.
42. Smeulders JB, Blom C, Mellema J (1990) Linear viscoelastic study of lipid vesicle dispersions: Hard-sphere behavior and bilayer surface dynamics. *Phys Rev A* 42(6):3483–3498.
43. Evans E, Yeung A (1994) Hidden dynamics in rapid changes of bilayer shape. *Chem Phys Lipids* 73(1):39–56.
44. De Haas K, et al. (1997) Rheological behavior of a dispersion of small lipid bilayer vesicles. *Langmuir* 13(25):6658–6668.
45. Belyy V, Kamaraju K, Akitake B, Anishkin A, Sukharev S (2010) Adaptive behavior of bacterial mechanosensitive channels is coupled to membrane mechanics. *J Gen Physiol* 135(6):641–652.
46. Häse CC, Le Dain AC, Martinac B (1995) Purification and functional reconstitution of the recombinant large mechanosensitive ion channel (MscL) of Escherichia coli. *J Biol Chem* 270(31):18329–18334.

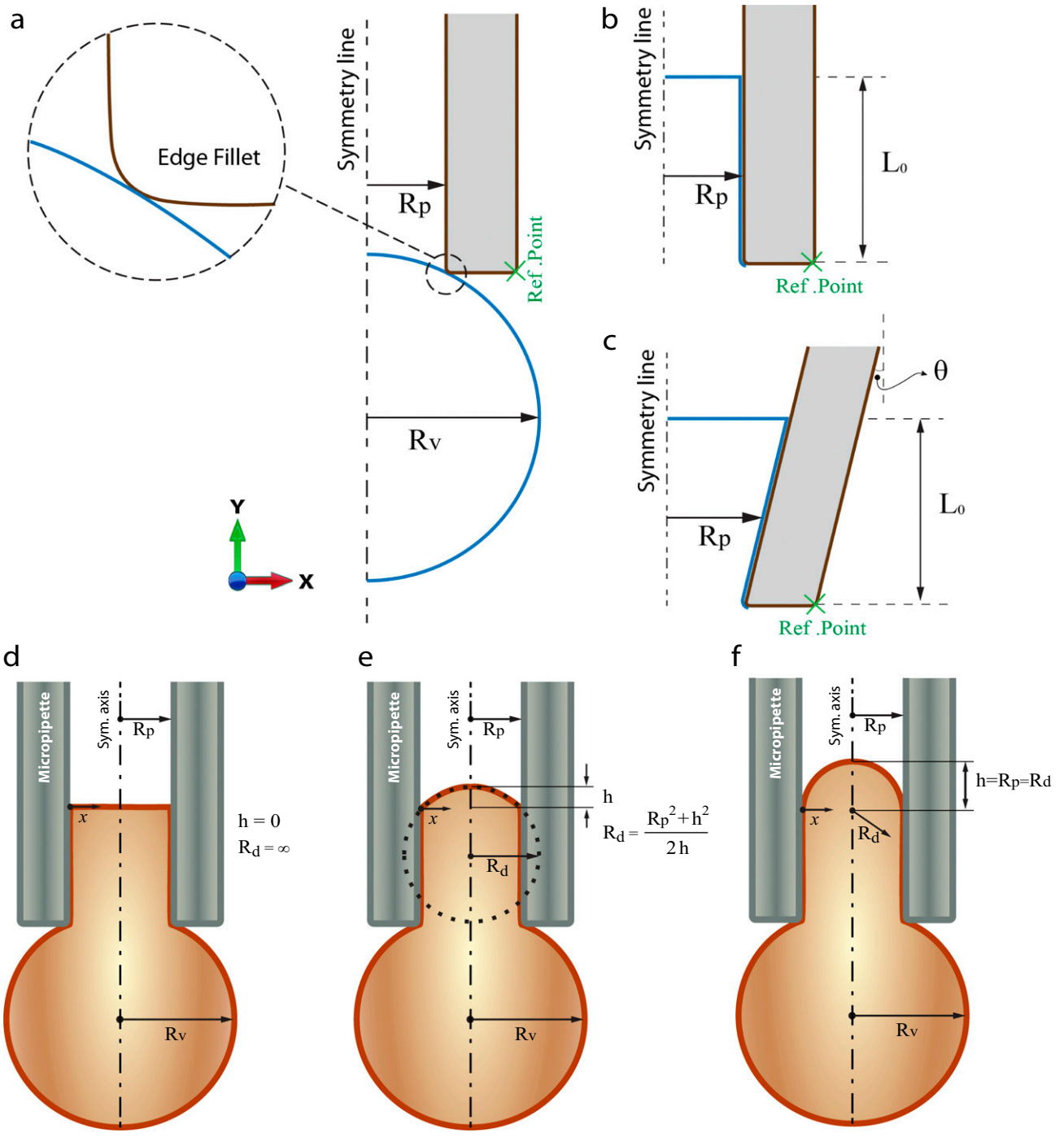

Fig. S1. Finite-element (FE) model of a lipid bilayer and a micropipette including schematic diagrams of the geometry of cell-attached micropipette aspiration. (*A*) For the FE model of cell-attached configuration, a liposome is modeled as a 2D axisymmetric semicircle with the radius of R_v. R_p is the inner radius of the micropipette. An edge fillet at the opening of the micropipette is used to mimic the experimentally used micropipettes and to avoid element distortion in this region. (*B* and *C*) FE model of excised patch membrane, where the lipid bilayer is modeled as a thin shell in flat form according to the realistic prestressed shape of the lipid bilayer at resting state, within a cylindrical pipette with the radius R_p, and a tapering pipette with the normal angle of θ, respectively. (*D*) Flat state of the patch area when the adhesion tension is much higher than the tension caused by the applied pressure within the pipette. (*E*) A general state of the patch area. R_d is the radius of the dome (radius of curvature), which can be calculated from the geometry of the patch using $((R_p^2+h^2)/2h)$; h is the height of the patch dome. (*F*) A special case where the adhesion tension is negligible and thus the patch area has a hemispherical shape.

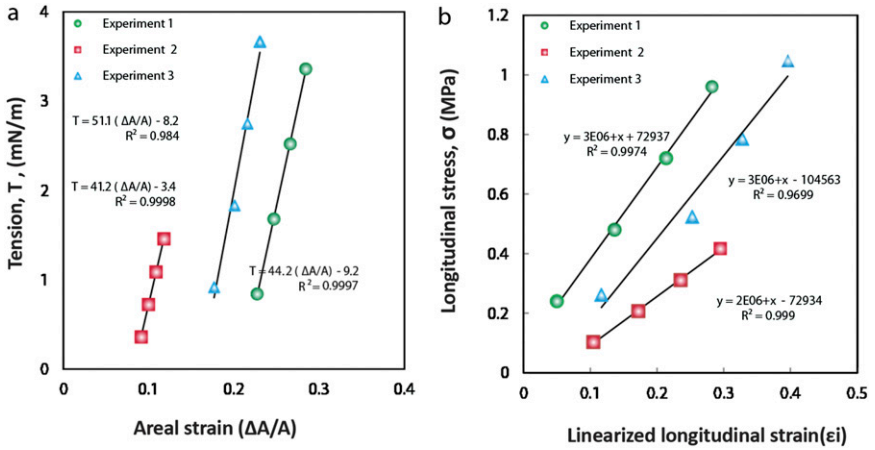

Fig. S2. Patch fluorometry results for three azolectin lipid vesicles of similar diameter (6–8 μm). (*A*) Variation of the membrane tension plotted against corresponding areal strain. Shown is how the membrane tension changes almost linearly with respect to areal strain; plots are fitted with linear regression lines. (*B*) Variation of the nominal longitudinal in-plane membrane stress vs. the linearized longitudinal strain fitted with linear regression lines. The diagram demonstrates the almost linear change of the nominal stress–strain field in the longitudinal direction.

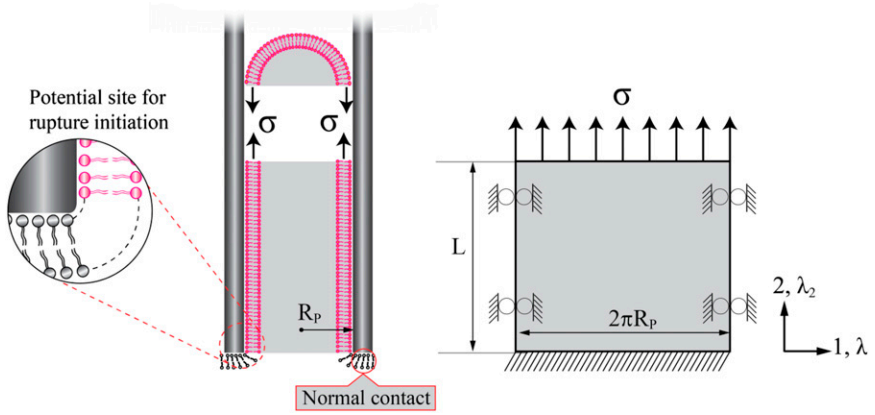

Fig. S3. Membrane stresses and boundary conditions of the lipid bilayer during a micropipette aspiration experiment. R_P and σ represent the inner radius of the pipette and the longitudinal stress of the membrane, respectively. λ_1 and λ_2 are the stretching ratios in directions 1 (horizontal) and 2 (vertical), respectively. L is the length of projection of the lipid within the micropipette. (*Right*) The planar form of a liposome with the associated boundary conditions caused by the rigid micropipette. (*Left*) The normal contact area between the liposome and the micropipette as well as one of the potential regions for rupture initiation in the liposome during micropipette aspiration.

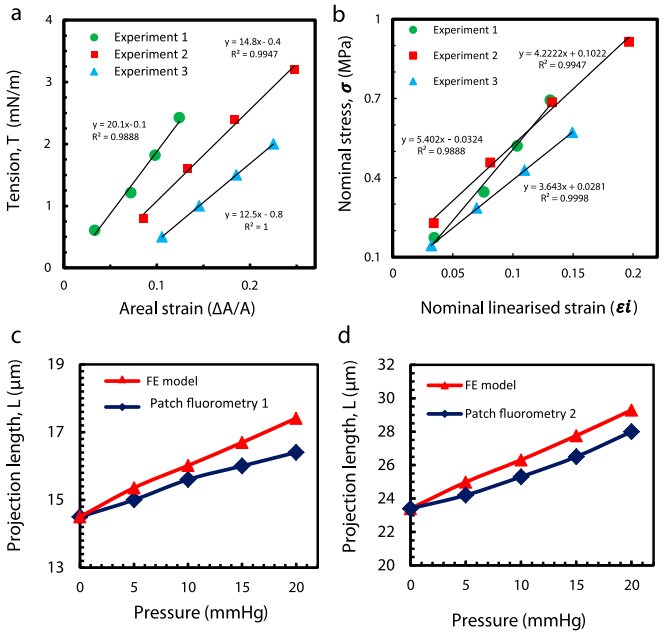

Fig. S4. Patch fluorometry results for three excised membrane patches and validation of simulations with observations from patch fluorometry experiments. (*A*) Variation of the membrane tension plotted against corresponding areal strain. Shown is how the membrane tension changes almost linearly with respect to the areal strain in the excised configuration; plots are fitted with linear regression lines. (*B*) Alteration of the nominal longitudinal in-plane membrane stress vs. the linearized longitudinal strain fitted with linear regression lines. The diagram demonstrates the almost linear change of the nominal stress–strain field in the longitudinal direction. (*C* and *D*) Comparisons between the measured aspiration lengths of azolectin lipid within the pipette and those simulated using the neo-Hookean hyperplastic model. The inner diameters of the micropipette are typical sizes encountered experimentally. The suction begins from 0 and reaches a value of −20 mmHg (−5 mmHg increments) instantaneously (in 0.01 s) and is then kept constant for 0.01 s. The computations are performed for the material parameters of $C_{10} = 0.71$ MPa and $k_b = 5.36 \times 10^{-21}$.

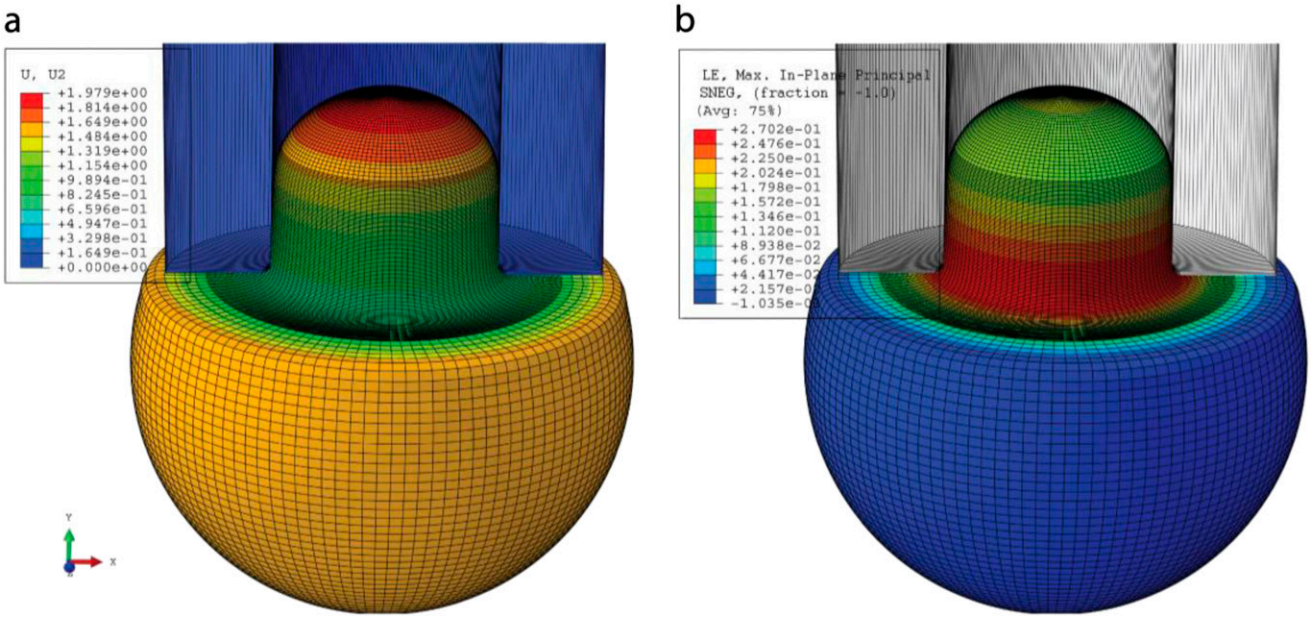

Fig. S5. Membrane stresses and displacement fields of lipid bilayer during a micropipette aspiration experiment. (*A*) Spatial profiles of the aspirated liposome calculated by FE simulation. The vesicle has a diameter of 6.2 μm. The inner diameter of the micropipette is 2.8 μm (both are typical sizes encountered experimentally). The suction begins from 0 and reaches a value of −30 mmHg (~4 kPa) instantaneously (in 0.01 s) and is then kept constant for 0.01 s. The computations are performed for the material parameters of $C_{10} = 0.5$ MPa and $k_b = 5.36 \times 10^{-21}$ J (neo-Hookean model). Shown are (*A*) the vertical displacement field (μm) and (*B*) in-plane maximum principal strain field in the azolectin vesicle.

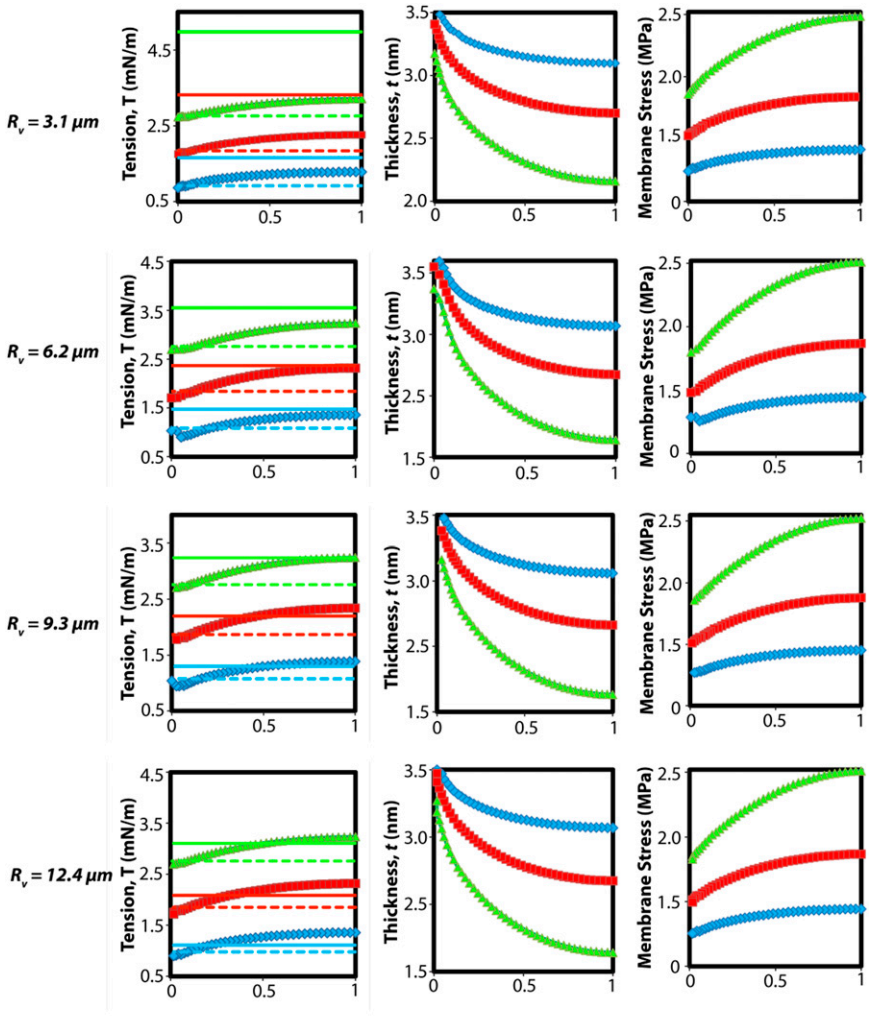

Fig. S6. FE results (tension, bilayer thickness, and in-plane stress) of a patch in the cell-attached configuration. The inner diameter of the micropipette is 2.8 μm (a typical size encountered experimentally). The suction begins from 0 and reaches a value of −30 mmHg (~4 kPa), instantaneously (in 0.01 s), and is then kept constant for 0.01 s. The computations are performed for the material parameters of $C_{10} = 0.5$ MPa and $k_b = 5.36 \times 10^{-21}$ J (model 3: neo-Hookean model). Each row shows the bilayer tension variation, the bilayer thickness change, and the membrane stress distribution within the patch area for different radii of vesicle, $R_v = 3.1$ μm (*First Row*), $R_v = 6.2$ μm (*Second Row*), $R_v = 9.3$ μm (*Third Row*), and $R_v = 12.4$ μm (*Fourth Row*). Solid line in *Left* column represents tension estimated using Eq. **S1** (cell-attached), and the dashed line represents tension estimated using Eq. **S18** (excised patch).

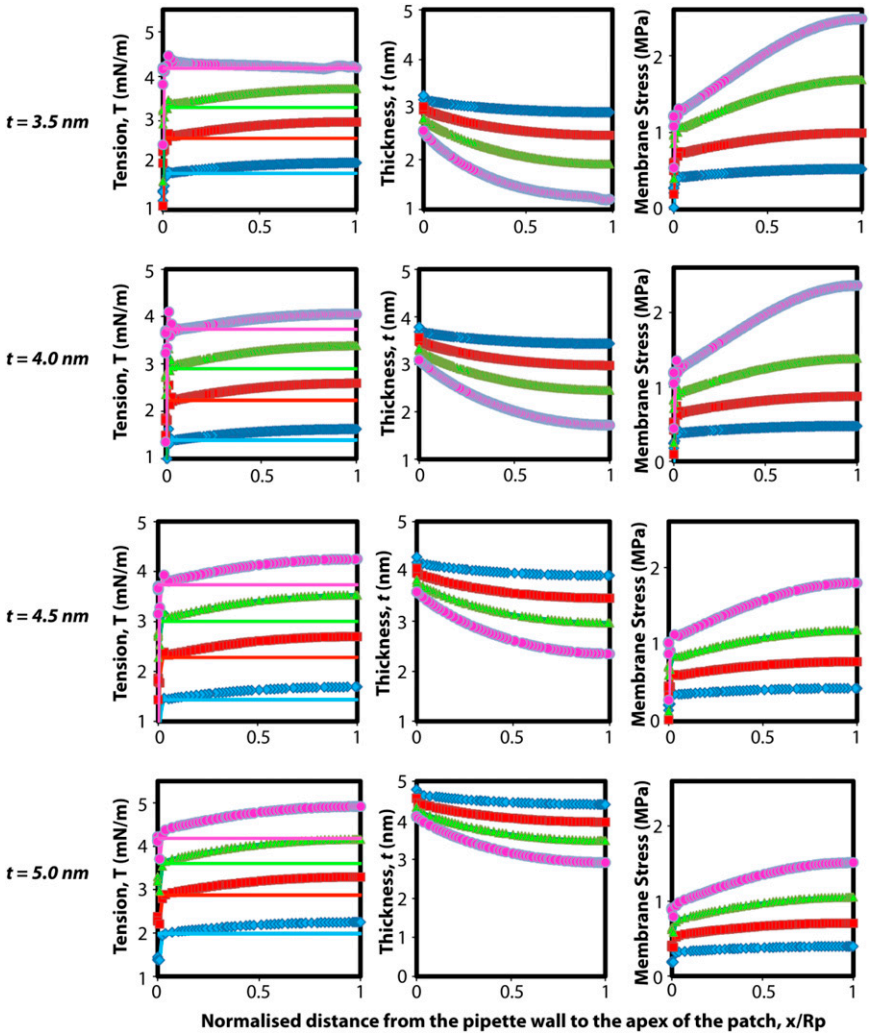

Fig. S7. Effect of initial thickness of bilayer on tension, thickness variations, and in-plane stress within the patch area in the excised patch configuration (using a cylindrical pipette). In these FE models, the inner diameter of the cylindrical micropipette is 2.8 μm (a typical size encountered experimentally). The suction begins from 0 and reaches a value of −40 mmHg (~5.3 kPa) instantaneously (in 0.01 s) and is then kept constant for 0.01 s. The computations are performed for the material parameters of $C_{10} = 0.5$ MPa and $k_b = 5.36 \times 10^{-21}$ J (neo-Hookean model). Each row shows the bilayer tension variation, the thickness change, and the membrane stress distribution within the patch area for different bilayer thicknesses, $t = 3.5$ nm (*First Row*), $t = 4$ nm (*Second Row*), $t = 4.5$ nm (*Third Row*), and $t = 5$ nm (*Fourth Row*). Solid lines in *Left* column represent tension estimated using Eq. **S18** (excised patch).

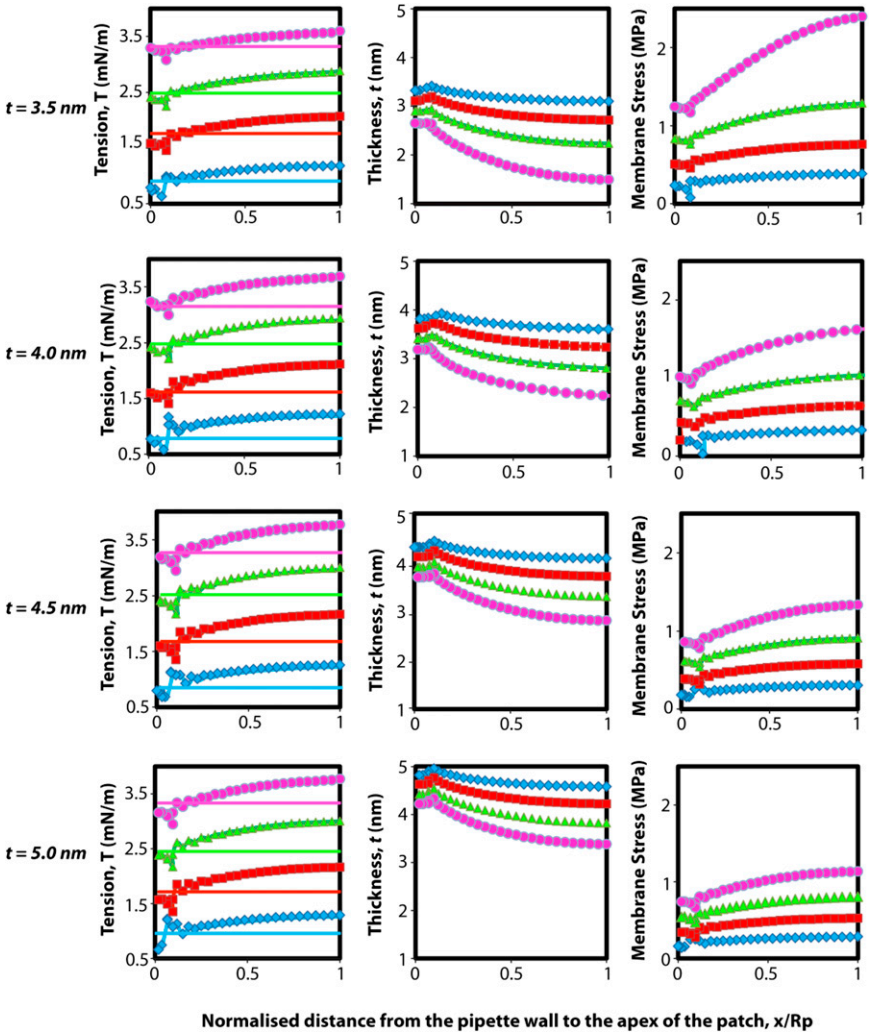

Fig. S8. Effect of initial thickness of bilayer on tension, thickness variations, and in-plane stress within the patch domain in excised patch configuration (using a conical pipette). All of the model properties are the same as those of the patch model with a cylindrical pipette (Fig. S7), except that the initial inner diameter of the conical micropipette is 1.2 μm before applying suction and the angle of the pipette is 10° (these are typical values encountered experimentally). Thus, the suction begins from 0 and reaches a value of −40 mmHg (~5.3 kPa) instantaneously (in 0.01 s) and is then kept constant for 0.01 s. The computations are performed for the material parameters of C_{10} = 0.5 MPa and $k_b = 5.36 \times 10^{-21}$ J (neo-Hookean model). Each row shows the bilayer tension variation, the thickness change, and the membrane stress distribution within the patch area for the bilayer thickness, $t = 3.5$ nm (*First Row*), $t = 4$ nm (*Second Row*), $t = 4.5$ nm (*Third Row*), and $t = 5$ nm (*Fourth Row*). Solid lines in *Left* column represent tension estimated using Eq. **S18** (excised patch).

Table S1. Validation of the proposed material properties of azolectin liposomes by comparing computational and experimentally derived values of the change in projection length, Δ*L*, at two different pressures (μm)

Different approaches	Δ*L*, in −10 mmHg	Δ*L*, in −20 mmHg
FE: linear elastic, model 1	0.4	0.6
FE: linear elastic, model 2	0.7	1.2
FE: neo-Hookean, model 3	0.8	1.6
Patch fluorometry experiment	0.8	1.7

Table S2. Pretension in the lipid within the pipette before pressurizing

Experiment no.	Excised patch	Cell-attached, small vesicles	Cell-attached, large vesicles
1	0.1	8.2	5.3
2	0.4	3.4	13.2
3	0.8	8.2	—

Extrapolations back to zero area dilation gave a value for the tension in the resting membrane of up to 13 ± 3 mN/m for very large vesicles, in close agreement with earlier measurements. Pretension values for the excised patch configuration may indicate the adhesion tension between the glass and azolectin lipid bilayer, whereas those of the vesicles are not just attributable to the adhesion tension. As can be seen, the pretensions in excised patches are much lower than those found in vesicles. All values are in mN/m.

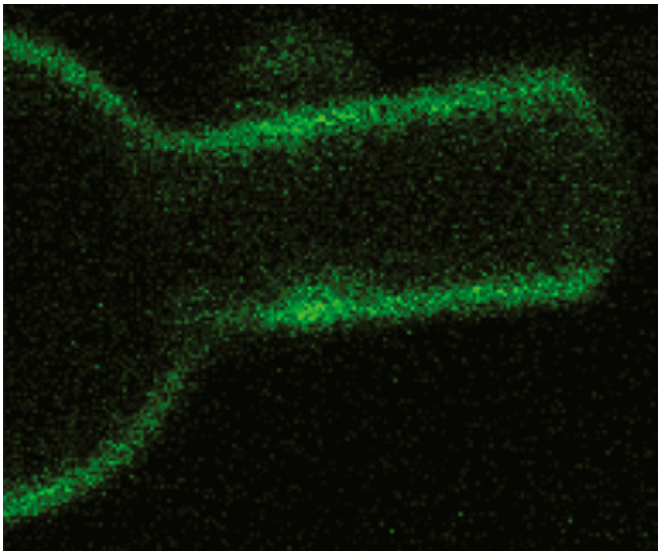

Movie S1. Movement of fluorescent-labeled azolectin liposomes (cell-attached configuration) during micropipette aspiration using confocal microscopy. Liposomes were aspirated by applying a negative pressure of −20 mmHg (5-mmHg increments).

Movie S1

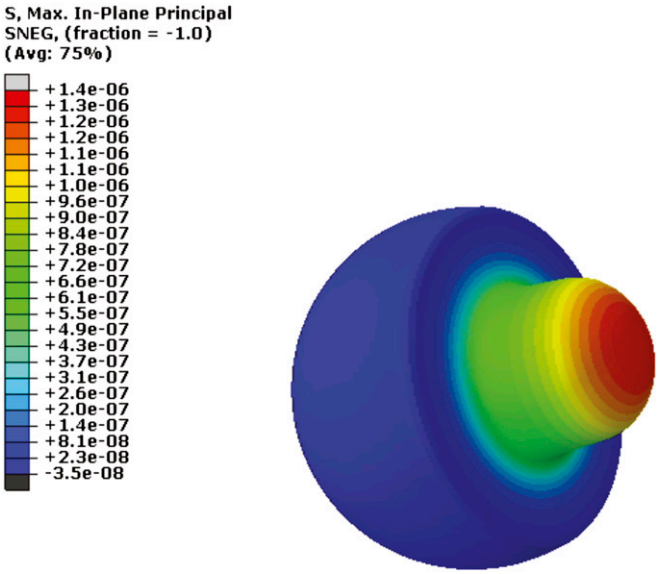

Movie S2. Simulation of the movement of a liposome patch (cell-attached configuration) and stress distribution during micropipette aspiration, using the finite-element method. A hyperelastic material model has been adopted here.

Movie S2

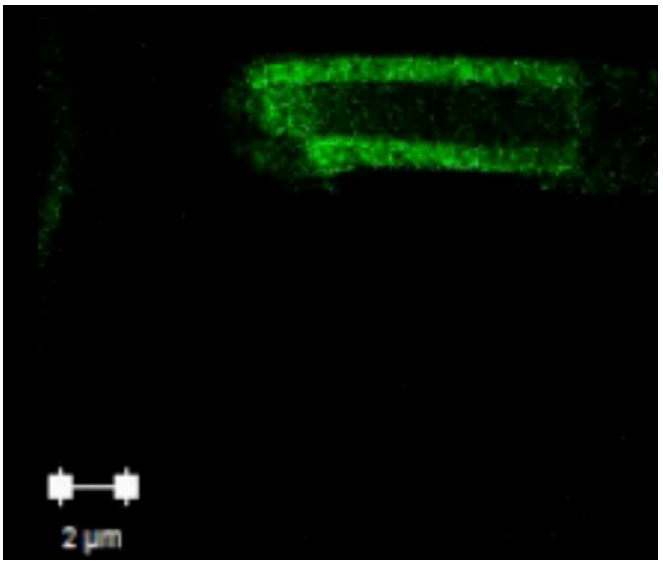

Movie S3. Movement of fluorescent-labeled azolectin lipid (excised patch configuration) during micropipette aspiration, using confocal microscopy. The membrane patches were aspirated by applying a negative pressure of −20 mmHg (5-mmHg increments).

Movie S3

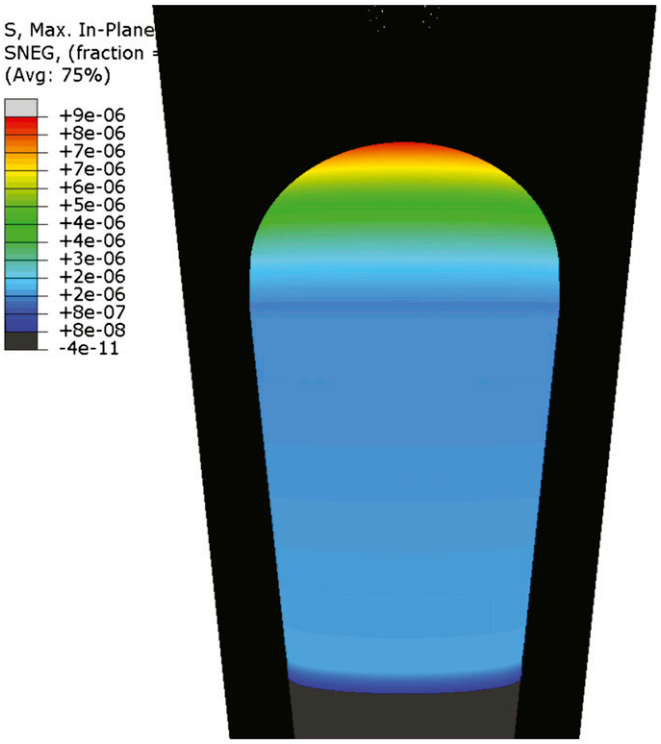

Movie S4. Simulation of the movement of azolectin lipid (excised patch configuration) and stress distribution during patch clamping, using the finite-element method. A hyperelastic material model has been adopted here.

Movie S4

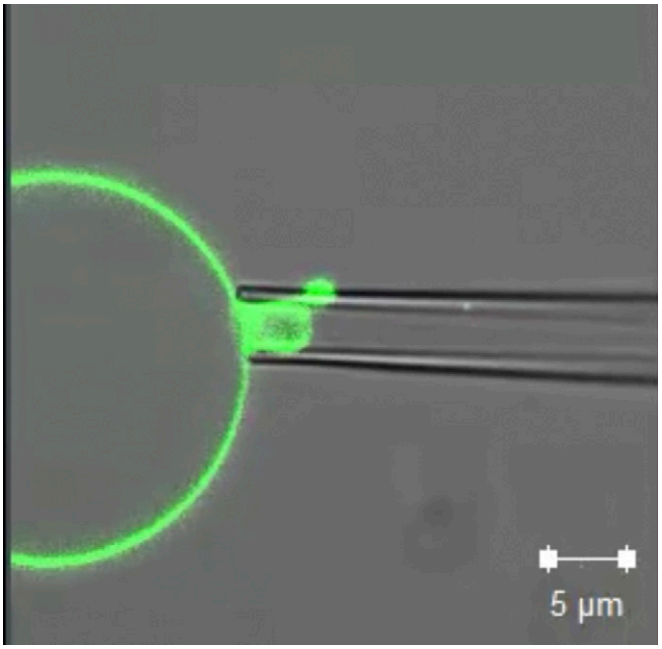

Movie S5. Movement of fluorescent-labeled azolectin liposome (cell-attached configuration) during aspiration, using a micropipette coated with 0.1% BSA. Liposomes were aspirated by applying a negative pressure of −15 mmHg (ramp) and then the pressure was released stepwise.

Movie S5

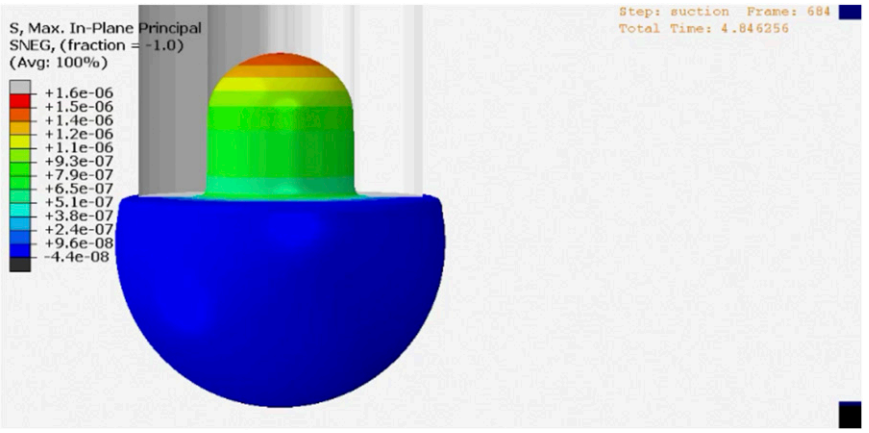

Movie S6. Simulation of the movement of a liposome patch (cell-attached configuration) and stress distribution during micropipette aspiration, using the finite-element method. The material model is visco-hyperelastic.

Movie S6

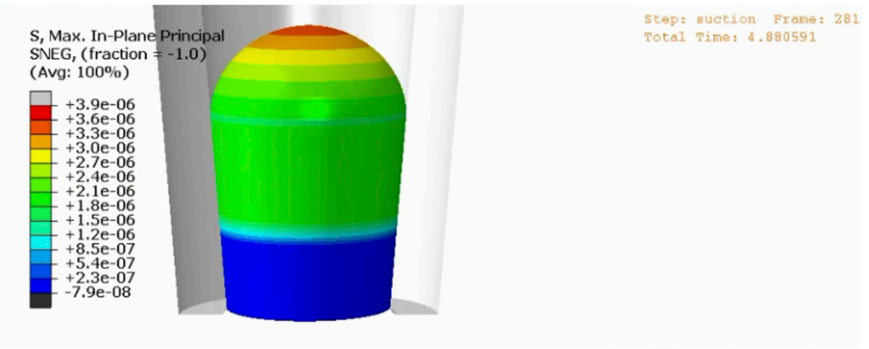

Movie S7. Simulation of the movement of a liposome patch (excised patch configuration) and stress distribution during patch clamping, using the finite-element method. The material model is visco-hyperelastic.

Movie S7